Supporting Information

Strontium doping RuO_2 electrocatalyst with abundant oxygen vacancies for boosting OER performance

Bei An [a], Xiaoqian Li [a], Yuan Lin [a], Fanfan Shang [a], Huijie He [a], Hairui Cai [a], Xiaoxiao Zeng [a], Weitong Wang [a], Shengchun Yang *[a,b,c], Bin Wang *[a,b,c]

[a] MOE Key Laboratory for Non-equilibrium Synthesis and Modulation of Condensed Matter, Key Laboratory of Shaanxi for Advanced Materials and Mesoscopic Physics, State Key Laboratory for Mechanical Behavior of Materials, School of Physics, Xi'an Jiaotong University, No. 28 West Xianning Road, Xi'an 710049, China

[b] National Innovation Platform (Center) for Industry-Education Integration of Energy Storage Technology, Xi'an Jiaotong University, No. 28 West Xianning Road, Xi'an 710049, China

[c] Shaanxi Collaborative Innovation Center for Hydrogen Fuel Cell PerformanceImprovement, Xi'an Jiaotong University, No. 28 West Xianning Road, Xi'an 710049, China

E-mail: ysch1209@mail.xjtu.edu.cn; bin_wang@xjtu.edu.cn

Experimental Section

Chemicals and Materials: Ruthenium chloride hydrate ($RuCl_3$, 99.99%) was purchased from J&K Scientific. Ethylene glycol ($(CH_2OH)_2$) was purchased from Tianjin Fuyu Fine Chemical Co., Ltd. Strontium nitrate ($Sr(NO_3)_2$, 99.5%), citric acid ($C_6H_8O_7$) and ethanol absolute (C_2H_6O) were purchased from Sinopharm Chemical. Nafion (5 wt%, DuPont) was purchased from commercial suppliers. The Milli-Q water of 18.2 MΩ·cm was used in all experiments. All chemicals were used directly without further purification.

Synthesis of Sr-doped RuO_2: The samples of Sr-doped RuO_2 were prepared by the sol-gel method followed by a calcination treatment. Briefly, 18 mg of $RuCl_3$ was first dissolved in 1 mL 0.5%vol C_2H_6O solution. Then, 1 mL solution containing 2.1 mg $Sr(NO_3)_2$ and 21 mg of $C_6H_8O_7$ was added into the above $RuCl_3$ solution under stirring to form a homogeneous solution, and the mixture was evaporated to dryness with continuous stirring at 150 ^oC. Finally, the obtained solid sample was calcinated in the furnace at different temperatures (*i.e.*, 350 ^oC, 450 ^oC, 550 ^oC, respectively). After cooling to room temperature, the synthesized samples were collected and assigned as $Sr_{0.1}RuO_x$-T (T = 350, 450, and 550, respectively). The reference sample of RuO_2 was prepared *via* the same method except for the addition of $Sr(NO_3)_2$ during the synthesis process.

Physicochemical characterizations: The powder X-ray diffraction (PXRD) analysis of the samples was conducted by using a Bruker D8 ADVANCE instrument equipped with Cu Kα radiation (λ=1.5418 Å) operating at 40 kV and 40 mA. The morphologies

of the samples were examined by using a scanning electron microscope (SEM). For SEM imaging, the samples were prepared by mounting the powder onto a conductive adhesive tape. The microstructures and morphology were further investigated by using transmission electron microscopy (TEM) with a JEOL JEM-F200 instrument, as well as high-angle annular dark-field scanning transmission electron microscopy (HAADF-STEM). In the case of TEM analysis, specimens were prepared by applying a dispersion of the sample onto a TEM grid. X-ray photoelectron spectroscopy (XPS) analysis was performed using the Thermo Fisher Scientific ESCALAB Xi+ spectrometer, employing a monochromatic Al Kα source with an energy of 1486.6 eV. The binding energy was calibrated by using the C 1s peak at 284.8 eV.

Electrochemical measurements: All the electrochemical testing was conducted in a three-electrode cell using a Cerrtest electrochemical workstation at 25 °C. The electrolyte was 0.5 M H_2SO_4 solution. During the electrochemical testing, an ink solution was prepared by adding 5 mg of catalyst into a solution containing 780 μL ethanol, 200 μL deionized water, and 20 μL Nafion. The resulting solution was subjected to ultrasonication for 30 minutes under an ice bath to ensure the formation of a homogeneous ink. The OER activity was measured by applying 5 μL of the ink onto a glassy carbon electrode, which served as the working electrode. A carbon rod was used as the counter electrode, while a saturated Hg/Hg_2SO_4 electrode served as the reference electrode. The OER activity was measured *via* linear sweep voltammetry (LSV), Tafel slope, and electrochemical impedance spectroscopy (EIS). The linear sweep voltammetry (LSV) was performed with a scan rate of 5 mV/s and 80% iR

correction. The Tafel plots were obtained from the LSV curves by fitting the linear portion of the Tafel plots. Electrochemical impedance spectroscopy (EIS) measurements were recorded in a frequency range from 0.1 to 10^4 Hz with an AC amplitude of 10 mV. The double-layer capacitances (C_{dl}) were calculated based on cyclic voltammetry (CV) curves, which were obtained by scanning the potential from 1.025 V - 1.125V *vs.* RHE (reversible hydrogen electrode), and the scanning rates were 5 mV/s, 25 mV/s, 50 mV/s, 75 mV/s, and 100 mV/s, respectively. The pH-dependence experiment was measured in electrolytes with different pHs, *i.e.*, 0.5 M H_2SO_4 (pH=0), 0.05 M H_2SO_4 (pH=1), and 0.005 M H_2SO_4 (pH=2), respectively. The same potential window was chosen of 1.1 V (*vs.* RHE) -1.5 V (*vs.* RHE). The OER stability was evaluated using a catalyst-loaded carbon cloth as the working electrode. To assess stability more comprehensively, a proton exchange membrane (PEM) electrolysis device was employed, 3 mg of as-prepared catalyst and 1.5 mg of commercial Pt/C were added to CP (1.5 × 1.5 cm), which served as the anode and cathode respectively, and the Nafion membrane (12 μm thick) acting as the solid polymer electrolyte. During the test, the electrolyte solution was supplied by a peristaltic pump. All potential was converted using the formula: $E_{RHE} = E_{Hg/Hg2SO4} + 0.652\ V + 0.059 \times pH$.

DFT calculations

All density functional theory (DFT) calculations were performed by using the Vienna Ab Initio Simulation Package (VASP).[24,25] To investigate the effects of Sr doping and oxygen vacancies, the models of $Sr_{0.1}RuO_2$, $Sr_{0.1}RuO_x$, and RuO_2 were built based on RuO_2 (110) planes. To ensure an appropriate surface vacuum, a vacuum layer

with a thickness of 15 Å was included in the vertical c-axis direction of the catalytic surfaces. A Monkhorst-Pack k-point mesh of 3×3×1 was employed for the model. Electron-electron and electron-ion interactions were described using the generalized gradient approximation (GGA) with the Perdew-Burke-Ernzerhof (PBE) functional.[26] The energy cut-off for the plane-wave basis set was set to 450 eV. The convergence criteria after relaxation is less than 10^{-5} eV $atom^{-1}$. The maximum number of steps for the electron self-consistent cycle was 60. During the structure optimization, the atoms in the top three layers of the surface were allowed to relax, while the atoms in the subsequent three layers were kept fixed to mimic the bulk behavior. The reaction Van der Waals interactions were taken into account when calculating the adsorption energies. The reaction path follows AEM as below:

$$*+ H_2O \rightarrow HO* + H^+ + e^- \quad (1)$$

$$HO* \rightarrow O* + H^+ + e^- \quad (2)$$

$$O* + H_2O \rightarrow HOO* + H^+ + e^- \quad (3)$$

$$HOO* \rightarrow O_2 + H^+ + e^- \quad (4)$$

In the above equation, the * represents the catalytic active site; H_2O, HO*, O*, and HOO* are the reaction intermediates. The Gibbs free energy changes are calculated using the equations:

$$\Delta G_{ads} = \Delta E_{ads} + \Delta ZPE - T\Delta S \quad (5)$$

Where ΔG_{ads}, ΔE_{ads}, ΔZPE, and ΔS represent the Gibbs free energy changes, the binding energy, zero-point energy changes, and entropy changes of the absorption process, respectively.

All calculations were performed at 298.15 K.

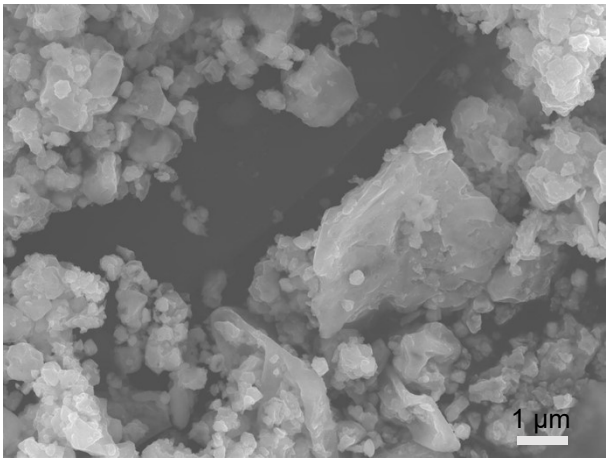

Fig. S1. SEM image of $Sr_{0.1}RuO_x$-450.

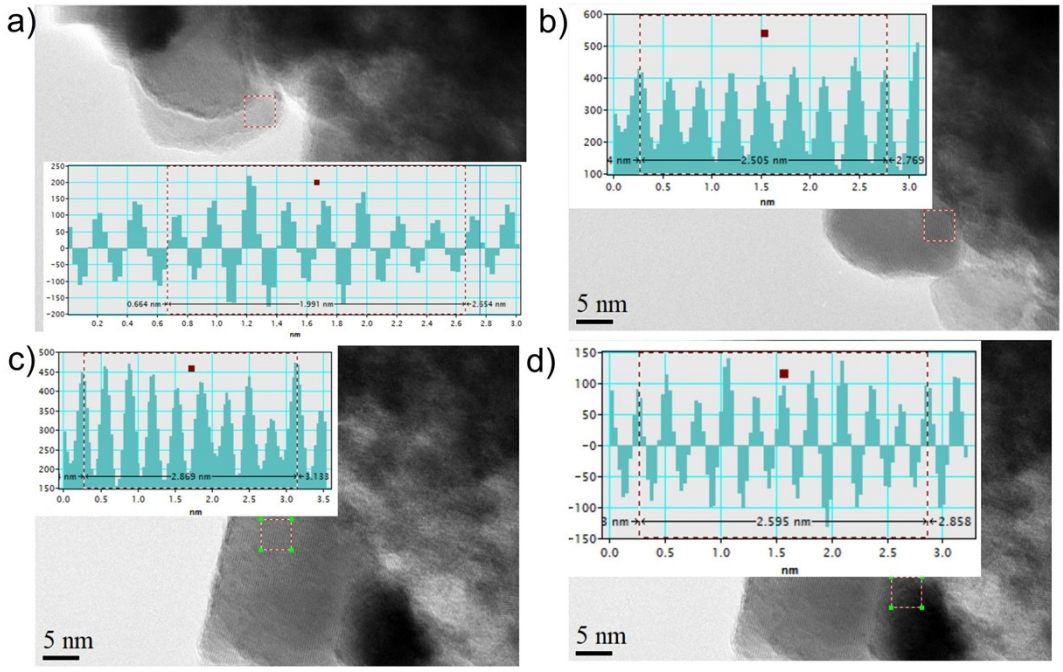

Fig. S2. The FFT inverse of a) RuO_2 (101) palne; b) RuO_2 (110) plane; c) $Sr_{0.1}RuO_x$ (110) plane; d) $Sr_{0.1}RuO_x$ (101) plane.

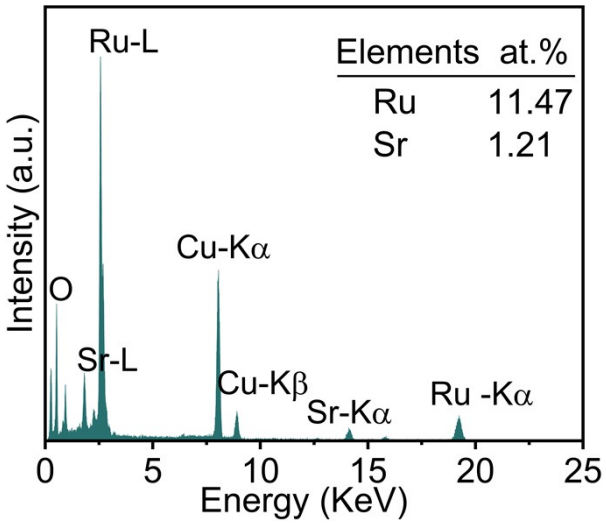

Fig. S3. EDS spectra of Sr, Ru, and O elements in the $Sr_{0.1}RuO_x$-450.

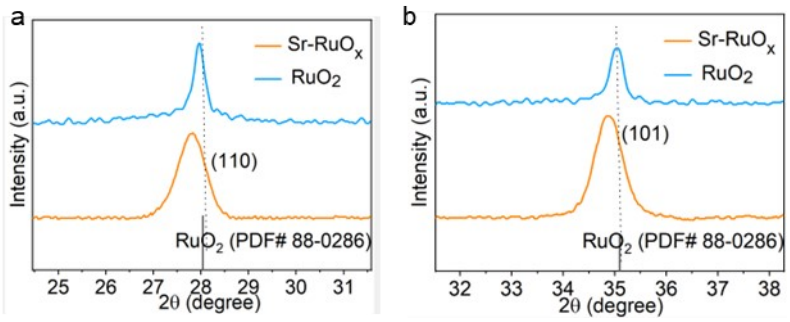

Fig. S4. PXRD pattern of the a) (110) plane and b) (101) plane for $Sr_{0.1}RuO_x$-450 and RuO_2.

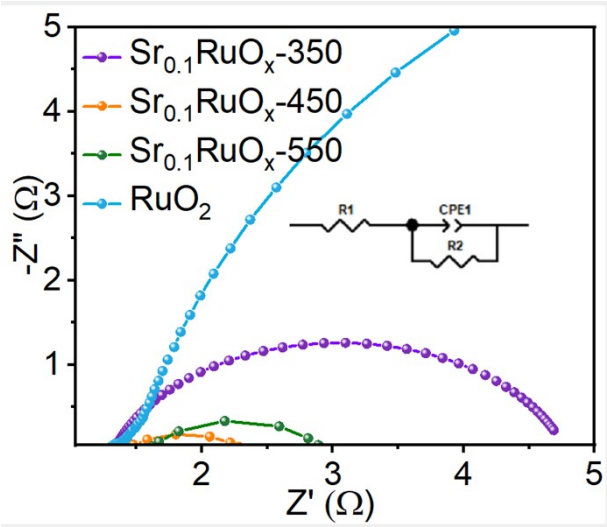

Fig. S5. EIS plots for RuO_2, $Sr_{0.1}RuO_x$-350, $Sr_{0.1}RuO_x$-450 and $Sr_{0.1}RuO_x$-550.

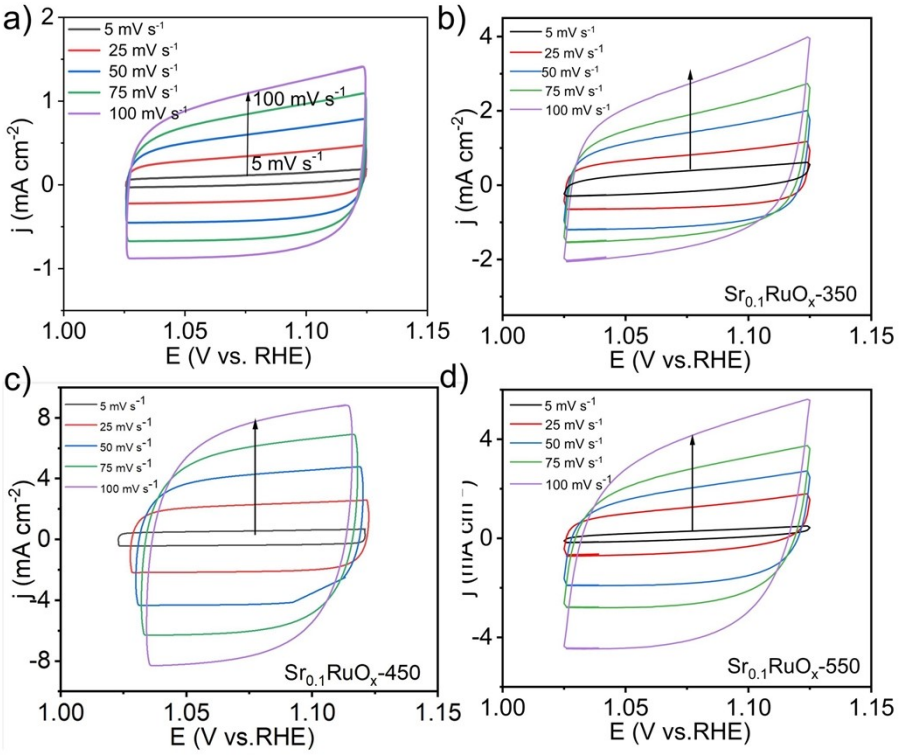

Fig. S6. Cyclic voltammetry curves for a) RuO_2, b) $Sr_{0.1}RuO_x$-350, c) $Sr_{0.1}RuO_x$-450, d) $Sr_{0.1}RuO_x$-550, respectively.

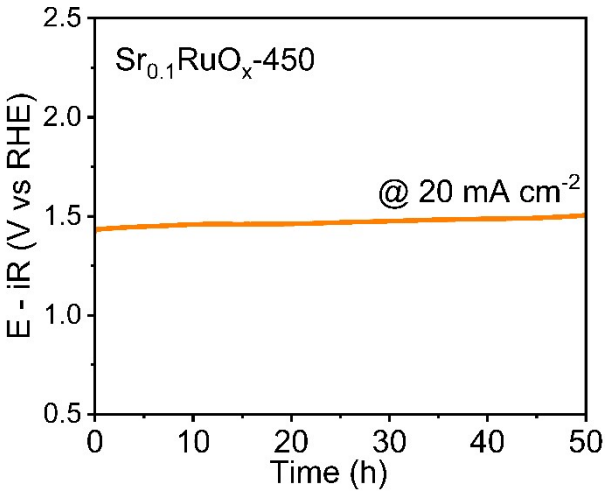

Fig. S7. Chronopotentiometry test of $Sr_{0.1}RuO_x$-450 at the current density of 20 mA cm^{-2}.

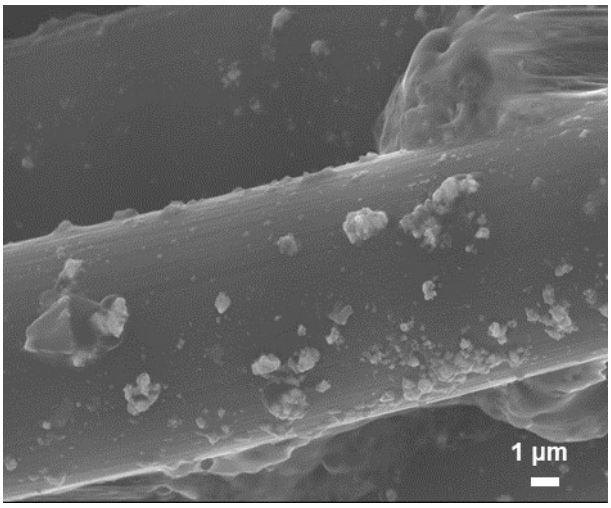

Fig. S8. The SEM on the carbon cloth after 100 h CP test.

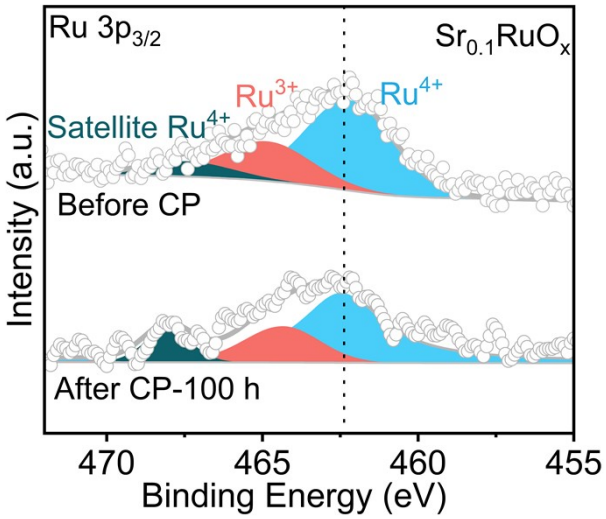

Fig. S9. Ru 3p XPS spectra of the $Sr_{0.1}RuO_x$-450 before and after the chronopotentiometry test.

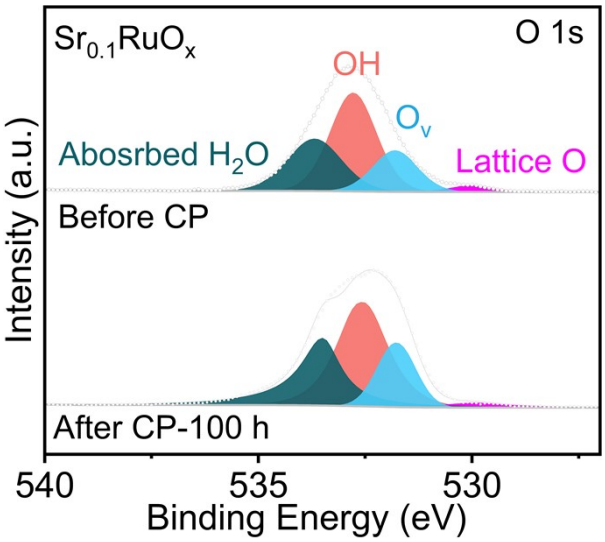

Fig. S10. O 1s XPS spectra of the $Sr_{0.1}RuO_x$-450 before and after the chronopotentiometry test.

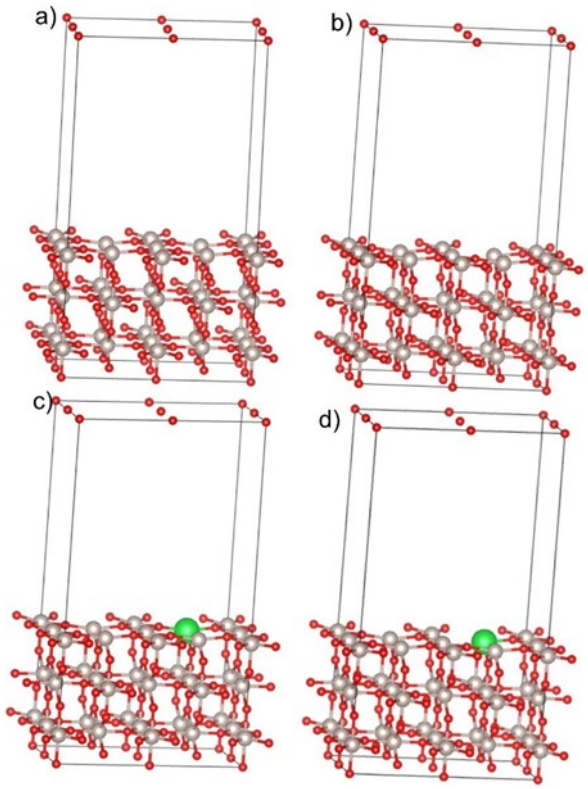

Fig. S11. The models of a) RuO_2, b) the RuO_2 with oxygen vacancies (RuO_x), c) the Sr doping RuO_2 ($Sr_{0.1}RuO_2$), and d) $Sr_{0.1}RuO_2$ with O vacancies ($Sr_{0.1}RuO_x$).

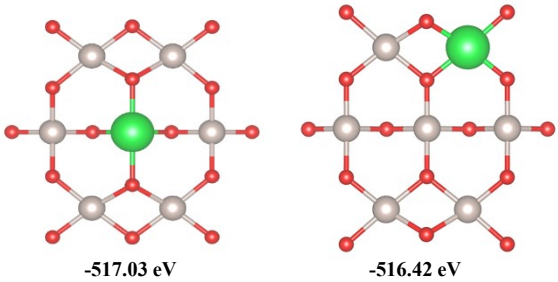

Fig. S12. Sr doped RuO_2 with different coordination.

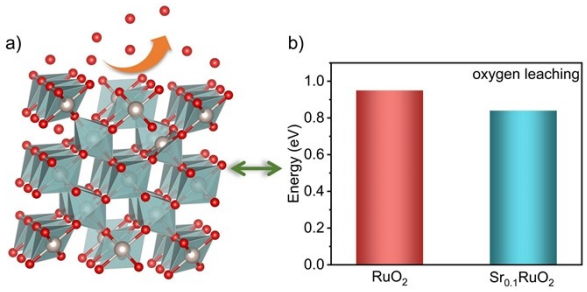

Fig. S13. a) The diagram of oxygen vacancy leaching; b) The $\Delta G_{O\ vacancy}$ for RuO_2 and $Sr_{0.1}RuO_2$.

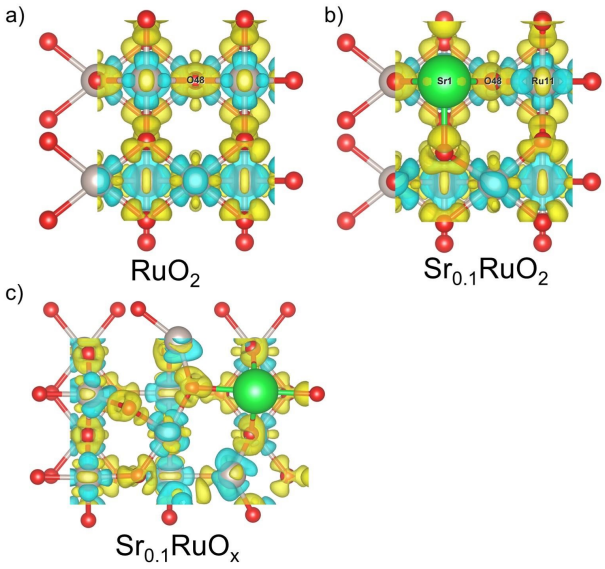

Fig. S14. The charge energy difference of a) RuO_2, b) $Sr_{0.1}RuO_2$, and c) $Sr_{0.1}RuO_x$; yellow and blue regions represent electron accumulation and depletion, respectively.

Table S1. Crystal parameters for RuO_2 and $Sr_{0.1}RuO_x$-450.

Sample	Ru-O (Å)	Ru-Ru (Å)	O-Ru-O(°)
RuO_2	2.02	3.14	93.81
$Sr_{0.1}RuO_x$-450	2.06	3.18	97.11

Table S2. Results of deconvolution of the Ru $3p_{3/2}$ XPS spectra of different catalysts in Figure 2c.

	RuO_2			**$Sr_{0.1}RuO_x$-450**		
	Ru^{4+}	Ru^{3+}	Sat.Ru^{4+}	Ru^{4+}	Ru^{3+}	Sat.Ru^{4+}
Peak position (eV)	462.1	464.7	467.1	462.3	464.9	467.4
FWHE (eV)	2.8	2.78	3.32	2.83	2.78	3.21
Peak areas	26744.3	16159.6	4059.5	2082.2	913.4	348.3
Proportion(to Ru^{4+})	1.65	1	0.25	2.28	1	0.38

	$Sr_{0.1}RuO_x$-450 (after CP-100 h)		
	Ru^{4+}	Ru^{3+}	Sat.Ru^{4+}
Peak position (eV)	462.5	464.4	468.0
FWHE (eV)	3.0	2.8	1.9
Peak areas	937.4	360.1	169.5
Proportion(to Ru^{4+})	2.63	1	0.47

Table S3. Results of deconvolution of the O 1s XPS spectra of different catalysts in the Figure 2d.

	RuO_2				$Sr_{0.1}RuO_x$-450			
	O_L-Ru	O_V	O_{OH}	H_2O	O_L-Ru	O_V	O_{OH}	H_2O
Peak position (eV)	530.2	531.8	532.8	533.9	529.8	531.7	532.3	533.7
FWHE (eV)	0.96	1.38	1.32	1.54	1.02	1.38	1.42	1.33
Peak areas	14935.9	48707.9	34670.8	6669.4	2005.5	13580.3	33402.8	20688
Proportion(to O_L-Ru)	1	3.26	2.32	0.45	1	6.77	16.66	10.31

Table S4. EIS fitting results of the components of the circuit shown in Figure 3d.

Catalysts	$Sr_{0.1}RuO_x$-350 / Error(%)	$Sr_{0.1}RuO_x$-450 / Error(%)	$Sr_{0.1}RuO_x$-550 / Error(%)	RuO_2 / Error(%)
R_s	1.6 / 0.47%	1.33 / 1.7%	1.6 / 0.84%	1.34 / 0.52%
R_{ct}	3.44 / 1.15%	0.9 / 7.38%	1.33 / 4.45%	12.76 / 0.91%
CPE-T	0.03 / 3.30%	0.08 / 6.72%	0.019 / 3.83%	0.012 / 1.70
CPE-P	0.8 / 1.06 %	0.72 / 4.76 %	0.49 / 4.15%	0.89 / 0.53%

Table S5. Comparison of overpotentials at 10 mA cm^{-2} and Tafel slopes for $Sr_{0.1}RuO_x$-450 and some reported high-efficient Ru-based electrocatalysts in acid electrolytes.

Catalysts	η_{10}(mV)	Tafel slope (mV dec^{-1})	Electrolytes	Reference
Sr-RuO_2	190	36.4	0.5 MH_2SO_4	This work
$Ru_{0.75}Mn_{0.2}O_{2-\delta}$	237	54.6	0.5 M H_2SO_4	[1]
Co-RuIr	235	66.9	0.1 M $HClO_4$	[2]
$Mn_{0.73}Ru_{0.27}O_{2-d}$	208	65.3	0.5 M H_2SO_4	[3]
Ru/S NSs	219	46.1	0.5 M H_2SO_4	[4]
Ru/RuO_2-Co_3O_4	226	49	0.1 M $HClO_4$	[5]
RuO_2/$(Co,Mn)_3O_4$	270	77	0.5 M H_2SO_4	[6]
RuMn NSBs	196	47.3	0.5 M H_2SO_4	[7]
B-RuO_2	200	55	0.5 M H_2SO_4	[8]
RuNi@G-250	227	65	0.5 M H_2SO_4	[9]
$Y_{1.8}Cu_{0.2}Ru_2O_7$	258	63	0.5 M H_2SO_4	[10]
Ru_1-N-C	267	52.6	0.5 M H_2SO_4	[11]
Ru_1-Pt_3Cu	220	52	0.5 M H_2SO_4	[12]
NPC@RuO_2	220	68.6	0.5 M H_2SO_4	[13]

References

[1] S. Chen, H. Huang, P. Jiang, K. Yang, J. Diao, S. Gong, S. Liu, M. Huang, H. Wang, Q. Chen, Ruthenium-manganese solid solution oxide with enhanced performance for acidic and alkaline oxygen evolution reaction, *ACS Catal*, 2022, **10**, 1152.

[2] J. Shan, T. Ling, K. Davey, Y. Zheng, S.-Z. Qiao, Transition-metal-doped RuIr bifunctional nanocrystals for overall water splitting in acidic environments, *Adv. Mater,* 2019, **31**, 1900510.

[3] K. Wang, Y. Wang, B. Yang, Z. Li, X. Qin, Q. Zhang, L. Lei, M. Qiu, G. Wu, Y. Hou, Highly active ruthenium sites stabilized by modulating electron-feeding for sustainable acidic oxygen-evolution electrocatalysis, *Energy Environ. Sci,* 2022, **15**, 2356.

[4] L. Liu, Y. Ji, W. You, S. Liu, Q. Shao, Q. Kong, Z. Hu, H. Tao, L. Bu, X. Huang, Trace lattice S inserted RuO_2 flexible nanosheets for efficient and long-term acidic oxygen evolution catalysis, *Small,* 2022, 2208202.

[5] T. Wang, Z. Li, H. Jang, M. G. Kim, Q. Qin, X. Liu, Interface engineering of oxygen vacancy-enriched Ru/RuO_2–Co_3O_4 heterojunction for efficient oxygen evolution reaction in acidic media, *ACS Sustain. Chem. Eng,* 2023, **11**, 5155-5163.

[6] S. Niu, X.-P. Kong, S. Li, Y. Zhang, J. Wu, W. Zhao, P. Xu, Low Ru loading RuO_2/$(Co,Mn)_3O_4$ nanocomposite with modulated electronic structure for efficient oxygen evolution reaction in acid, *Appl. Catal. B Environ,* 2021, **297**,120442.

[7] L. Li, L. Bu, B. Huang, P. Wang, C. Shen, S. Bai, T.-S. Chan, Q. Shao, Z. Hu, X. Huang, Compensating electronic effect enables fast site-to-site electron transfer over ultrathin RuMn nanosheet branches toward highly electroactive and stable water splitting, *Adv. Mater,* 2021, **33**.

[8] C. Liu, B. Sheng, Q. Zhou, D. Cao, H. Ding, S. Chen, P. Zhang, Y. Xia, X. Wu, L. Song, Motivating Ru-bri site of RuO_2 by boron doping toward high performance acidic and neutral oxygen evolution, *Nano Res,* 2022, **15**, 7008-7015.

[9] X. Cui, P. Ren, C. Ma, J. Zhao, R. Chen, S. Chen. N. P.Rajan, H. B. Li, L. Yu, Z. q. Tian, D. h. Deng, Robust interface Ru centers for high-performance acidic oxygen evolution, *Adv Mat*, 2020, **32**, 1908126.

[10] D. A. Kuznetsov, M. A. Naeem, P. V. Kumar, P. M. Abdala, A. Fedorov, C. R. Müller, Tailoring lattice oxygen binding in Ruthenium pyrochlores to enhance oxygen evolution activity, *J. Am. Chem. Soc*, 2020, **142**, 7883-7888.

[11] L. L. Cao, Q. Lu, J. J Chen, L. Wang, Y, Lin, H. J. Wang, X. K. Liu, X.y. Shen, W. Zhang, W. Liu, Z. M. Qi, Z. Jiang, J. L. Yang, T. Yao, Dynamic oxygen adsorption on single-atomic Ruthenium catalyst with high performance for acidic oxygen evolution reaction. *Nat Commun*, 2019, **10**, 4849.

[12] Y. Yao, S. Hu, W. Chen, Z.-Q. Huang, W. Wei, T. Yao, R. Liu, K. Zang, X. Wang, G. Wu, W. Yuan, T. Yuan, B. Zhu, W. Liu, Z. Li, D. He, Z. Xue, Y. Wang, X. Zheng, J. Dong, C.-R. Chang, Y. Chen, X. Hong, J. Luo, S. Wei, W.-X. Li, P. Strasser, Y. Wu, Y. Li, Engineering the electronic structure of single atom Ru sites via

compressive strain boosts acidic water oxidation electrocatalysis, *Nat. Catal*, 2019, **2**, 304-313.
[13] J. Y. Yu, G. X. Li, H. Liu, L. L. Zhao, A. z. Wang, Z. Liu, H. d. Li, H. Liu, Y. Y. Hu, W. J. Zhou, Ru–Ru_2PΦNPC and NPC@RuO_2 synthesized via environment-friendly and solid-phase phosphating process by saccharomycetes as N/P sources and carbon template for overall water splitting in acid electrolyte, *Adv. Functional. Mat*, 2019, **29**, 1901154.